Neuron
Case Study

Plasticity and Stability of the Visual System in Human Achiasma

Michael B. Hoffmann,[1] Falko R. Kaule,[1,11] Netta Levin,[4,11] Yoichiro Masuda,[5] Anil Kumar,[6] Irene Gottlob,[6] Hiroshi Horiguchi,[5,7] Robert F. Dougherty,[7] Joerg Stadler,[9] Barbara Wolynski,[1] Oliver Speck,[2] Martin Kanowski,[3] Yaping J. Liao,[8] Brian A. Wandell,[7] and Serge O. Dumoulin[10,*]
[1]Department of Ophthalmology
[2]Department of Biomagnetic Medical Magnetic Resonance and Physics
[3]Department of Neurology
Otto-von-Guericke-University, 39120 Magdeburg, Germany
[4]Department of Neurology, Hadassah Hebrew University Medical Center, 91120 Jerusalem, Israel
[5]Department of Ophthalmology, Jikei University School of Medicine, 105-8461 Tokyo, Japan
[6]Department of Ophthalmology, University of Leicester, Leicester LE2 7LX, UK
[7]Department of Psychology, Stanford University, Stanford, CA 94305-2130, USA
[8]Department of Ophthalmology, Stanford University, Stanford, CA 94303-5353, USA
[9]Leibniz Institute for Neurobiology, 39118 Magdeburg, Germany
[10]Department of Experimental Psychology, Helmholtz Institute, Utrecht University, 3584CS Utrecht, The Netherlands
[11]These authors contributed equally to this work
*Correspondence: s.o.dumoulin@uu.nl
http://dx.doi.org/10.1016/j.neuron.2012.05.026

SUMMARY

The absence of the optic chiasm is an extraordinary and extreme abnormality in the nervous system. The abnormality produces highly atypical functional responses in the cortex, including overlapping hemifield representations and bilateral population receptive fields in both striate and extrastriate visual cortex. Even in the presence of these large functional abnormalities, the effect on visual perception and daily life is not easily detected. Here, we demonstrate that in two achiasmic humans the gross topography of the geniculostriate and occipital callosal connections remains largely unaltered. We conclude that visual function is preserved by reorganization of intracortical connections instead of large-scale reorganizations of the visual cortex. Thus, developmental mechanisms of local wiring within cortical maps compensate for the improper gross wiring to preserve function in human achiasma.

INTRODUCTION

Ordered maps of the contralateral visual field are presumed imperative for proper visual system function and are a core principle of the notion of hemispheric specialization (Huberman et al., 2008; Wandell et al., 2007). A prerequisite for this map formation in animals with binocular vision is a partially crossed projection of the optic nerves at the optic chiasm. Here, axons from the nasal and temporal retinae are guided by molecular markers to the contralateral and ipsilateral hemisphere, respectively (Petros et al., 2008). There they form a retinotopic map of the visual hemifield contralateral to the respective hemisphere (Figure 1A and see Figure S1, available online). In congenital achiasma, this crossing is absent providing large-scale erroneous input to the visual system (Apkarian et al., 1994, 1995; Victor et al., 2000; Williams et al., 1994). Both hemiretinae project to the ipsilateral hemisphere, which as a consequence receives input not only from the contralateral, but also from the ipsilateral visual hemifield. This poses a substantial challenge to the organization of visual field maps and prompts potential sensory conflicts. Despite these sizable aberrant projections, achiasmic humans have relatively normal visual function (Apkarian et al., 1994, 1995; Prakash et al., 2010; Victor et al., 2000). Therefore achiasma offers a unique opportunity to study the principles governing cortical map development in humans. The knowledge of cortical mapping in this condition would provide insights into scope and mechanisms of developmental plasticity in the human visual system.

The organization of the visual cortex and of the visual pathways beyond the lateral geniculate nucleus (LGN) in achiasma is unknown as only very few studies addressed related issues (Victor et al., 2000; Williams et al., 1994). A study in a canine model of achiasma investigated the precise mapping of information in the visual system, but it was confined to the level of the LGN. Here retinotopic maps of opposing hemifields in adjacent LGN layers were revealed (Williams et al., 1994). Another pioneering study addressed the cortical organization in human achiasma using functional magnetic resonance (fMRI) (Victor et al., 2000). This case study suggested that stimuli in opposing visual hemifields are represented in close cortical vicinity, but visual field map representations could not be reconstructed. To date the geniculostriate projections (LGN-striate or optic radiations), cortico-cortical projections and the corresponding cortical organization pattern are still obscure in achiasma, such that the developmental mechanisms that make the abnormal visual input available for visual perception remain unknown. An idea of the cortical organization patterns to be expected,

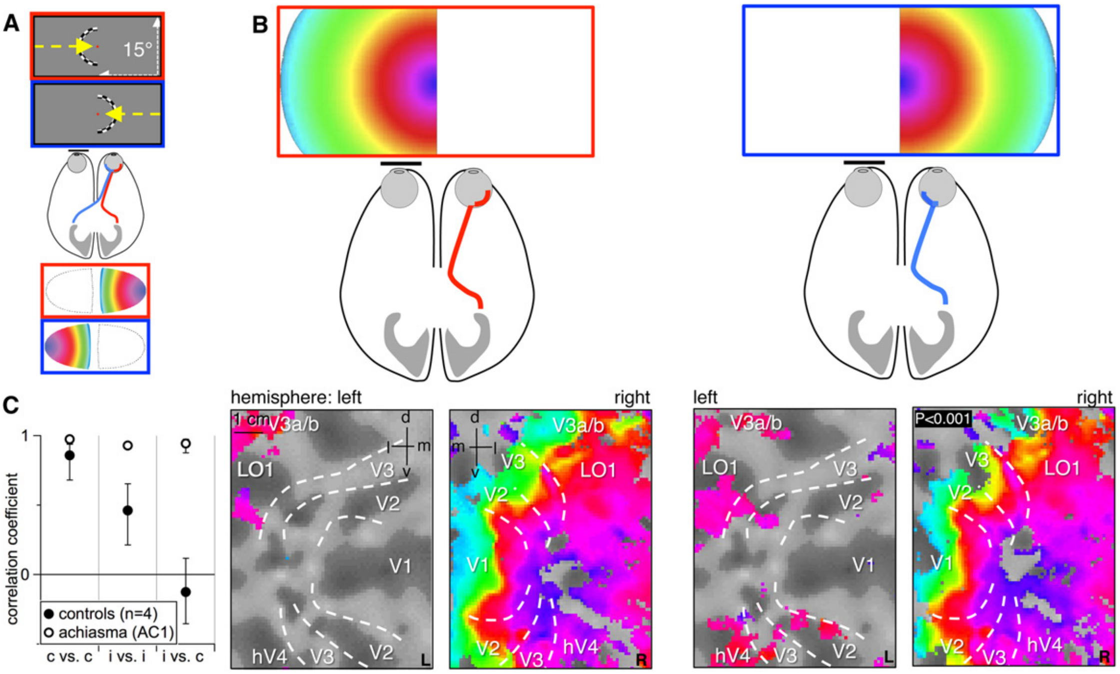

Figure 1. Hemifield Retinotopic Mapping Results

(A) Schematic of the normal projection pattern of the optic nerve of the right eye together with the visual contracting ring stimulus for hemifield eccentricity mapping and its color-coded representation in a schematic V1-flatmap. The nasal retina (blue) projects to the contralateral and the temporal retina (red) to the ipsilateral hemisphere, resulting in a representation of each hemifield on its respective contralateral hemisphere.

(B) Schematic of the achiasmic optic nerve projection and eccentricity maps in AC1's flattened representation of the early visual areas upon separate monocular stimulation of the right eye in the left and right visual hemifield. Responses are dominant in the right hemisphere and organized as an orderly eccentricity map for both visual hemifields. The visual area boundaries are indicated as determined from polar angle mapping (Figure S1).

(C) Correlation of the respective hemifield mappings to quantify the cortical superposition of hemifield maps in right V1 (mean ± SD across four controls and for AC1 across repetitive correlations). In the controls the two repetitions of contralateral hemifield mappings were correlated ($p < 0.01$) and, to a lesser degree ($p < 0.04$), also those of two repetitions of ipsilateral hemifield mappings, but, in contrast, not those of contra- and ipsilateral field mappings. For AC1 both contra- and ipsilateral field mappings were highly correlated ($p < 0.001$). See also Figure S1.

Abbreviations: V, visual area; LO, lateral occipital area; d, dorsal; v, ventral; m, medial; l, lateral; R, right hemisphere; L, left hemisphere; c, visual hemifield contralateral to right V1; i, visual hemifield ipsilateral to right V1.

however, can be inferred from visual field representations in albinism, where part of the temporal retina projects abnormally to the contralateral hemisphere (Guillery, 1986). Thus, input from both hemifields reaches each hemisphere. In fact, in albinism three different resulting cortical organization patterns have been reported. The geniculostriate projection can be reordered resulting in a contiguous retinotopic map of both visual hemifields (''Boston'' pattern); alternatively, reordering can be absent with intracortical suppression inducing a lack of behavioral sensitivity of the temporal retina (''Midwestern'' pattern) or without suppression retaining sensitivity (''True Albino'' pattern). While the former organization patterns of the visual cortex appear to be reserved to nonprimate models of albinism, the latter is found in both nonprimates and primates (Guillery et al., 1984; Hoffmann et al., 2003). Our aim was to resolve the organization pattern in human achiasma.

We investigated two of these extremely rare achiasmic subjects. Three types of investigations were performed using 1.5, 3, and 7 Tesla MRI: (1) optimized retinotopic mapping (DeYoe et al., 1996; Engel et al., 1994, 1997; Hoffmann et al., 2009; Sereno et al., 1995; Wandell et al., 2007), (2) characterization of the population receptive field (pRF) properties (Dumoulin and Wandell, 2008), and (3) diffusion-tensor imaging (DTI) and tractography to investigate white matter integrity (Sherbondy et al., 2008a, 2008b). Our results indicate that the abnormal visual input in human achiasma does not induce a sizable topographic reorganization in the geniculostriate projection or of the occipital callosal connections. We propose that reorganization of intracortical architecture in the visual system underlies the ability to cope with these abnormal inputs.

RESULTS

Hemifield Mapping Reveals Overlapping Visual Field Maps

In subject AC1, visual hemifield representations on the cortical surface were obtained separately for each visual hemifield and eye using fMRI-based retinotopic mapping (DeYoe et al., 1996; Engel et al., 1994, 1997; Hoffmann et al., 2009; Sereno et al., 1995; Wandell et al., 2007). Mapping of either visual hemifield yielded dominant responses on the occipital lobe ipsilateral to the stimulated eye (Figures 1 and S1). Figure 1 illustrates that stimulation of the right eye revealed orderly eccentricity maps of both hemifields on the right hemisphere only (Figure 1B). Moreover, opposite visual hemifields were represented as a cortical superposition of mirror-symmetrical visual field positions. Accordingly, the phase maps obtained for stimulation in opposite hemifields were highly correlated (Figure 1C) and the borders of the early visual areas were identical for the representation of the contralateral and the ipsilateral visual hemifield as derived from polar angle maps (Figure S1). Similar results were obtained on the left hemisphere for stimulation of the left eye (Figure S1).

PRF Mapping Reveals Bilateral Population-Receptive Fields

The above results predicted that in the visual cortex of achiasmic humans, neural populations within an fMRI recording site have bilateral receptive fields (population receptive fields, pRFs), receiving distinct inputs from the contra- and the ipsilateral visual hemifield. To test this directly, we extended a model-based data-analysis technique to estimate the properties of the pRF (Dumoulin and Wandell, 2008). The stimuli consisted of moving-bar apertures covering both visual hemifields. The conventional pRF model consists of a circularly symmetric 2D Gaussian, whose resulting parameter estimates vary systematically across visual cortex and match closely to nonhuman primate electrophysiology (Amano et al., 2009; Dumoulin and Wandell, 2008; Harvey and Dumoulin, 2011; Winawer et al., 2010). We compared four models of the pRF: the conventional 2D Gaussian pRF model and three additional models that consisted of two 2D Gaussians. The two 2D Gaussians were identical, except that their positions were either mirrored around the vertical meridian, fixation, or horizontal meridian. Because all parameters of the two Gaussians were linked, these new models have the same degrees of freedom as the conventional one Gaussian pRF model, i.e., the model performance can be compared directly. But unlike the conventional model, the three alternate models predict that each cortical location responds to stimuli from two distinct regions of visual space. We compared the four models by computing the average goodness-of-fit, i.e., variance explained, within the right Calcarine sulcus. Both achiasmic subjects were included in this analysis.

For both achiasmic subjects in the right Calcarine sulcus, the pRF model consisting of two Gaussians mirrored across the vertical-meridian explained most of the variance, whereas for control subjects the conventional pRF model explained most of the variance in the data (Figure 2A). Inspection of individual fMRI time series of the achiasmic subject (AC2), indicate that the pRF model consisting of two Gaussians captures systematic signal modulations that the conventional model cannot explain (Figures 2B and 2C). These improvements are evident for most individual recording sites across the cortical surface extending beyond V1, again in contrast with control subjects (Figures 2D and 2E). Another line of evidence supporting the notion that achiasmic subjects have symmetric pRFs both in contra and ipsilateral visual hemifield comes from pRF sizes. The pRF size properties are comparable to controls, only when considering the atypical pRF model consisting of two Gaussians mirrored across the vertical meridian (Figures 2F and S2). The pRF sizes across early visual cortex in conjunction with the persistence of dual receptive fields into extrastriate cortex, also implies relatively unaltered cortico-cortical connections (Harvey and Dumoulin, 2011).

DTI and Tractography Reveal Relatively Normal White Matter Tracts

Since each hemisphere contains information of the whole visual field in achiasma, we questioned whether the two hemispheres needed to communicate to the same degree. Therefore, we investigated the visual pathway connectivity including the occipital callosal connections. A previous study demonstrated the sensitivity of these connections to alterations of the visual input (Levin et al., 2010). Visual pathways white matter analysis was performed in two steps: identifying the fiber bundles and evaluating their properties. Using a new probabilistic algorithm (Sherbondy et al., 2008a, 2008b), we could clearly identify the *optic tract* and the *optic radiation* composing the input fibers to the visual cortex as well as the output fibers from each hemisphere, which cross at the corpus callosum (Figure 3A). Following fiber identification, we studied white matter integrity using directional diffusivity measures. By measuring diffusivity in multiple directions we obtained estimates of the principal diffusion direction (longitudinal) as well as the perpendicular direction (radial). The ratio of these two values is similar to the fractional anisotropy (FA). We found that the properties of the achiasmic subject's (AC2) visual pathways were within the range of 30 normally sighted control subjects (Figure 3B). Finally, the cross-sectional area of the occipital fibers that connect right and left visual cortex was assessed (Figure 3C). In normal sighted controls, there is a correlation between the cross-sectional area of this tract and the cross-sectional area of the entire callosum. The cross-sectional area of the achiasmic subject's occipital callosal fiber group was smaller than that of controls, yet the overall size of his corpus callosum was small too (Figure 3D). These results highlight that the white matter integrity at the resolution of our neuroimaging measurements is comparable to control subjects.

DISCUSSION

Our results highlight both differences and similarities of the achiasmic compared to the typical human visual system. In achiasma, we found a highly atypical organization of the visual cortex consisting of overlapping visual hemifield maps with bilateral pRFs. In contrast, pRF sizes were in the normal range as were the properties of all major visual pathways, in particular the geniculate-cortical and occipital-callosal fibers. Moreover, normal pRF sizes across early visual cortex in conjunction with the persistence of bilateral pRFs imply relatively unaltered cortico-cortical connections (Harvey and Dumoulin, 2011).

Conservative Geniculostriate Projections in Human Achiasma

Our results can be explained by conservative developmental mechanisms in human achiasma that largely preserve the normal visual pathways beyond the LGN. Both retinotopic and pRF mapping demonstrated an overlay of orderly retinotopic maps from opposing hemifields in the visual cortex, such that each cortical location represents two separate visual field locations,

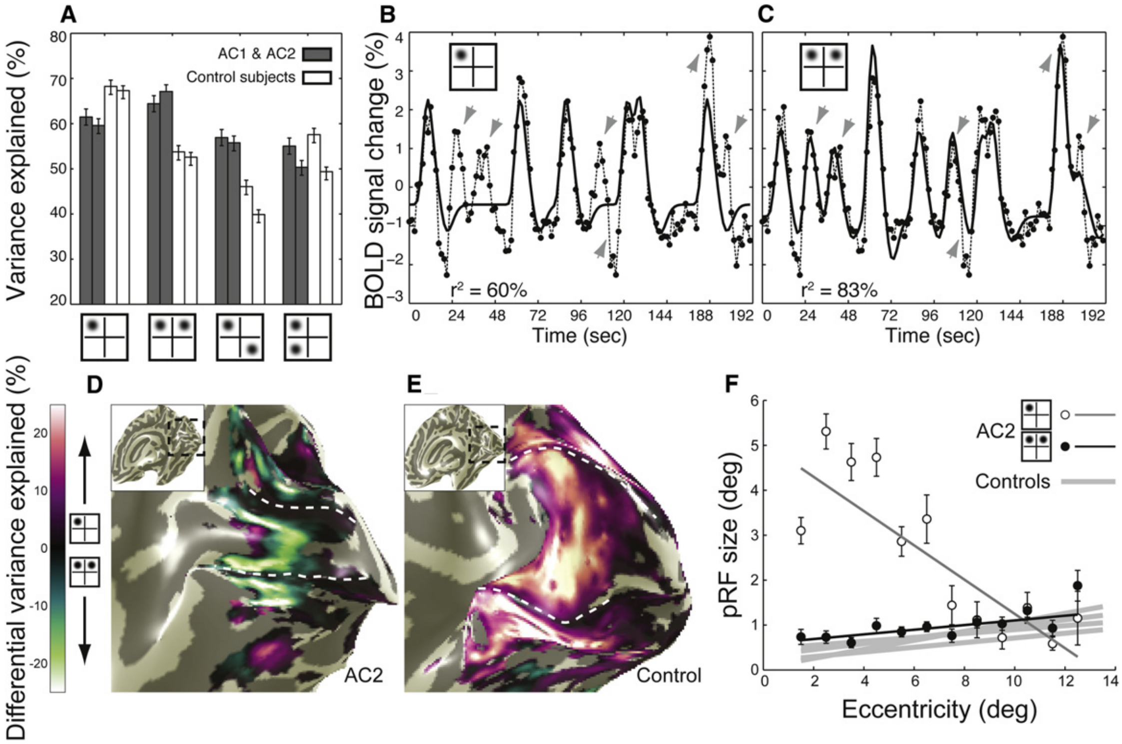

Figure 2. Population Receptive Field Modeling Results

(A) pRF model comparisons for AC1 and AC2 (left and right, respectively) and two control subjects at the respective measurement sites. The mean variance explained and 95% confidence intervals for fMRI responses in the right Calcarine sulcus are shown for four different pRF models. Only cortical locations where any model explains more than 50% of the variance are included the analysis. However, the results are near-identical for any other or no threshold. Four different models were tested: the conventional pRF model containing 1 Gaussian and three different pRF models with 2 Gaussians where the Gaussians are mirrored around the y axis, fixation or x axis. The pRF models are indicated by the x axis's cartoon representations. There is no difference in degrees of freedom in the models. In the right hemisphere of the achiasmic subjects, the model containing 2 pRFs mirrored around the y axis explains most of the variance. In control subjects, the conventional model explains most of the variance in the data. Two example pRF model fits are shown in (B) and (C). These panels show the fMRI data of AC2 (dotted line) fitted (solid line) with a conventional pRF using a single Gaussian (B) and a 2 Gaussian pRF model (C). The insets indicate the particular pRF model that is fitted to the data and the variance explained (r^2). The conventional pRF model consistently misses certain time-series features that are captured by the 2 Gaussian pRF model (gray arrows). Next, we compared the conventional pRF model to the pRF model consisting of 2 Gaussians mirrored on the y axis by subtracting the variance explained of either model. The difference in percent variance explained of both models is shown on the cortical surfaces of AC2 (D) and a control subject (E). The data that is shown has at least a variance explained of 30% in any pRF model. The dashed white lines indicate the V1–V2 border (vertical meridian or y axis). In the subject without an optic chiasm, the pRF model with two Gaussians mirrored on the y axis explains most of the variance within and beyond V1, whereas in the control subject the conventional model explains most of the variance in the fMRI data.

(F) pRF size versus eccentricity in the right Calcarine sulcus of AC2 (mean ± SEM) and 4 control subjects. In the control subjects pRF sizes increase with eccentricity (Dumoulin and Wandell, 2008). This relationship is also plotted for the subject without an optic chiasm for two pRF models (conventional model: open circles; pRF model consisting of two Gaussians mirrored on the y axis: closed circles). The pRF sizes of the conventional pRF model deviate from the known relationship between (p)RF size and eccentricity in humans and animals, but the pRF sizes of the novel two Gaussian pRF model are consistent with the known relationship as illustrated by control subjects.

See also Figure S2.

namely one in each hemifield. This intermixed representation could result from individual neurons with bilateral receptive fields, but also from the interdigitation of two different neural populations representing the contra- and ipsilateral visual field at the current fMRI resolution. These two neural representations are not mutually exclusive. In support of the latter, behaviorally achiasmic subjects do not make any obvious confusion between visual hemifields in line with previous reports (Victor et al., 2000). Furthermore, Williams et al. (1994) demonstrated that in the only animal model of achiasma, the Belgian sheepdog, the different layers of the LGN receive input from the ipsilateral eye of either the contra- or the ipsilateral visual hemifield. As a consequence, a conservative geniculostriate projection would yield interdigitated representations of the contra- and ipsilateral fields in V1, as those would occupy the former ocular dominance columns (Guillery, 1986; Huberman et al., 2008). This corresponds to the intermixed cortical visual field representations we observed. Thus, the data are in support of largely conservative geniculostriate pathways in achiasma preserving the normal gross topography of the projections. This is further corroborated by the normal gross anatomy of the optic radiations as determined using DTI and tractography. It should be noted, however, that the data do not speak to the fine-grained organization in V1 in achiasma. Thus, it is not clear whether the afferents from the

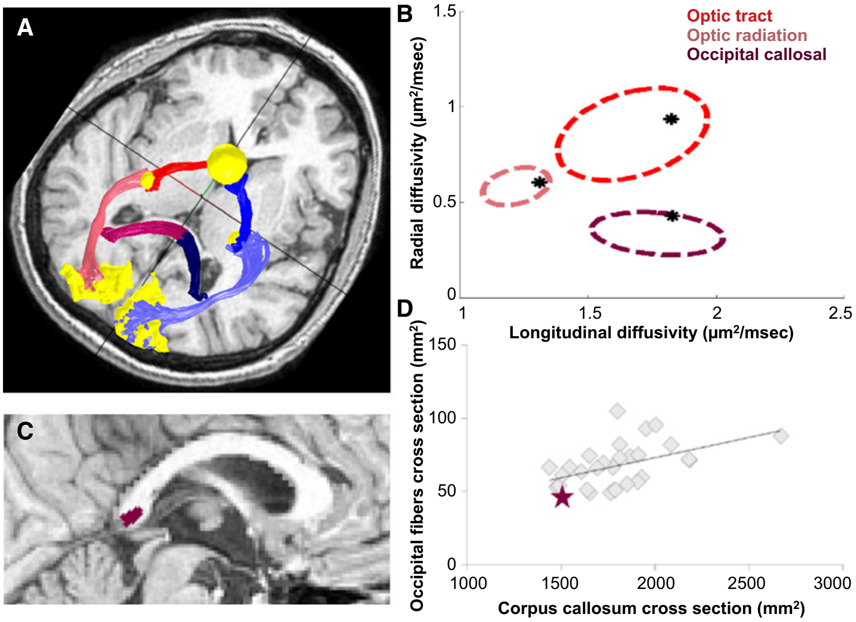

Figure 3. Diffusion Tensor Imaging (DTI) and Tractography Results of AC2 and 30 Controls

(A) ROIs and estimated fiber bundles superimposed on the T1 weighted axial slice, viewed from below. Estimates of the right (red) and left (blue) optic tracts; the right (pink) and left (purple) optic radiations; the right (dark red) and left (dark blue) occipital callosal fibers. Yellow spheres represent the optic chiasm (large anterior) LGN's (small in the middle) and Calcarine sulcus (posterior) regions of interest.

(B) Scatter plot of the radial and longitudinal diffusivities of the optic tract, optic radiation and occipital callosal fiber groups (see color legend on the right). The two standard deviation covariance ellipsoid of 30 normally sighted subjects is drawn for each fiber group. The black stars represent the averaged right and left diffusivity values for each fiber group in the achiasmic subject which are within the range of control subjects.

(C) The location of the occipital callosal fibers in the plane of the corpus callosum.

(D) Scatter plot of the cross-sectional area of the occipital callosal fiber group in relation to the cross-sectional area of the entire corpus callosum. The cross-sectional area of achiasmic occipital callosal fiber group (purple star) is small compared to the controls (gray diamonds); however, the overall size of AC2′s corpus callosum is small too.

different LGN layers organize themselves into structures reminiscent of ocular-dominance columns, namely into hemifield columns. In conclusion, the highly atypical functional responses in V1 appear to be a consequence of the gross miswiring at the chiasm without corresponding changes in the gross wiring of the geniculostriate projection.

Conservative Cortico-Cortical Projections in Human Achiasma

Beyond V1, cortico-cortical connections remain stable as indicated by normal pRF sizes in both striate and extrastriate cortex (Harvey and Dumoulin, 2011) and the persistence of bilateral pRFs in extrastriate cortex. Even interhemispherical connections appear little affected, as stable normal occipital callosal connections were observed. The finding that the representation error in the LGN is propagated in an unaltered manner to the primary visual cortex and beyond highlights the dominance of conservative developmental mechanisms in human achiasma.

Developmental Mechanisms Associated with Visual Pathway Abnormalities

The mapping of the abnormal input observed in achiasma resembles that of human and nonhuman primates with completely different types of misrouting, namely abnormal crossing from the temporal retina in albinotic subjects (Guillery, 1986; Hoffmann et al., 2003) or an absence of crossing due to a prenatal hemispheric lesion (Muckli et al., 2009). In contrast, a variety of organization patterns in V1 have been reported for nonprimate albinotic animal models of misrouted optic nerves, part of which involves sizable remapping (Guillery, 1986). In the human visual cortex, such large scale remapping does not appear to be a prevalent strategy to avoid sensory conflicts (Hoffmann et al., 2007; Wolynski et al., 2010).

Visual Perception

Our results demonstrate a remarkable degree of both stability and plasticity in human achiasma. The observed cortical organization with overlapping visual hemifield maps with bilateral pRFs is highly atypical and the consequence of a large degree of stability in the geniculostriate and cortico-cortical projections. Still visual function is relatively unaffected, with the exception of nystagmus and the absence of stereopsis. In line with previously reported achiasmic subjects (Apkarian et al., 1994, 1995; Prakash et al., 2010; Victor et al., 2000), the subjects made effective use of their vision in daily life, including sport activities and reading. They performed normal on various clinical tasks, including largely normal visual field sensitivities and no visual field defects associated with the abnormal representation of the nasal retina. Further, there was no apparent confusion between left and right visual fields, in line with previous reports that have found no evidence for perceptual crosstalk across the opposing hemifields, neither in achiasma (Victor et al., 2000) nor albinism (Klemen et al., 2012).

In order to make the abnormally represented visual information available for perception, neural plasticity is required. We propose that instead of large-scale reorganizations, comparatively subtle intracortical mechanisms mediate the achiasmic subjects' ability to cope with the abnormal visual input. For example, normally binocular information is integrated to yield stereovision. In achiasma, however, these integrative mechanisms would result in major sensory conflicts such as confusions between the two hemifields. Plasticity of intracortical mechanisms is therefore required to selectively block such integrative processes while supporting others, e.g., those required to shape monocular spatial receptive field properties. Remarkably, conservative geniculostriate and cortico-cortical mapping of abnormal retinogeniculate input provides a sufficient scope of developmental plasticity in humans to make substantially abnormal representations available for relatively normal visual perception.

EXPERIMENTAL PROCEDURES

Subjects

Data of two male achiasmic patients and their respective controls were acquired at two sites, at Magdeburg University, Germany (AC1 and four controls), and Stanford University, USA (AC2 and 34 controls). The control subjects were visually and neurologically normal. The procedures followed the tenets of the declaration of Helsinki, and the participants gave their written consent. The ethical committees of the University of Magdeburg and the Stanford Institutional Review Board approved the respective protocols.

AC1 (aged 22) was referred with the clinical diagnosis of severe hypoplasia of the optic chiasm based on a T1 weighted MRI and functional achiasma was confirmed with VEPs (Apkarian et al., 1983, 1995). He made effective use of his vision including reading and the diagnosis of the chiasmic malformation was incidental (age 20). His best-corrected decimal visual acuity was 0.5 for the dominant right and 0.17 for the left eye, and there was no foveal hypoplasia. He had alternating exotropia (2 deg), dissociated vertical deviation (5 deg), and was stereoblind. Automated perimetry (Octopus 101 Perimeter; Haag-Streit, Koeniz, Switzerland) with optimized protocols (Hoffmann et al., 2007) revealed normal visual fields. Specifically, no visual field defects were associated with the nasal retina, and visual field sensitivities did not differ between nasal and temporal hemiretinae of the dominant right eye (mean sensitivities ± SEM [dB] for nasal and temporal hemiretina [n = 47 test locations each] 25.9 ± 0.37 and 25.5 ± 0.46, respectively; p = 0.48, paired t test). The subject exhibited normal visual and visuomotor behavior throughout testing. There was no left-right confusion as tested for saccadic eye movements (100% correct saccades to 12 targets in the right and 12 in the left visual hemifield, displaced laterally 5.8 deg from a central fixation target). Moderate see-saw nystagmus (around 3 deg horizontal and vertical amplitude for the right eye) was evident. It has been shown previously that fixation instabilities of such moderate extent have only little effect on the visual field map reconstruction (Baseler et al., 2002; Levin et al., 2010). The left eyes of the four male control subjects and both eyes of AC1 were stimulated monocularly during the retinotopic hemifield mapping experiments. A control's and AC1's right eye were also measured for pRF mapping.

AC2 (aged 30) has been described in detail in a previous publication (Prakash et al., 2010). In summary, the subject was born with a nonrandom association of birth defects know as VACTERL (*v*ertebral anomalies, *a*nal atresia, *c*ardiovascular anomalies, *t*racheosophageal fistula, *e*sophageal atresia, *r*enal and/or radial anomalies, and *l*imb anomalies). Appendicular abnormalities were surgically repaired. As a child, he had mild infantile nystagmus with relatively normal visual function. He had been diagnosed with attention deficit disorder as a child and bipolar affective disorder as an adult. Even so, he completed high school and worked full-time. He also made effective use of his vision, including during sport activities and reading. At 29, he was evaluated for a two-year history of gradually worsening headache, blurred vision, and increased nystagmus amplitude and the diagnosis of achiasma was made at this time by brain MRI and fMRI showing functional noncrossing of the visual pathway. On examination, his visual acuities were 1.0 and 0.8 in the right and left eye, respectively, with a small left relative afferent pupillary defect. Anterior and posterior segments were normal. The subject's eye movements had full duction, normal saccade latencies, amplitudes, and peak velocities. He exhibited pendular nystagmus and episodic seesaw nystagmus, which were relatively minimal during the current fMRI studies (age 30). Stereopsis was absent. Color perception was within normal limits per Hardy-Rand-Rittler pseudoisochromatic plates. There was no left-right confusion or neglect per clinical testing using visual stimuli in nasal or temporal fields or simultaneously to one or both eyes. Goldmann perimetry revealed slightly constricted visual fields bilaterally with no evidence of temporal or other visual field defect.

Hemifield Mapping

Visual Stimuli

For retinotopic hemifield mapping (DeYoe et al., 1996; Engel et al., 1994, 1997; Sereno et al., 1995) a section of a contrast reversing circular checkerboard stimulus (6 reversals/s, 90 cd/m^2 mean luminance) presented in a rectangular mask (30 deg wide and 15 deg high; Figure 1A) was used to stimulate monocularly either the nasal or the temporal retina in separate experiments. The stimulus contrast was set to 98% in the hemifield to be mapped and to 0% in the opposing hemifield. Seven 36 s cycles of the stimulus stepping either through the polar angles (clockwise and counterclockwise for the left and right hemifield, respectively) as a rotating wedge (90 deg) for polar angle mapping or through the eccentricities as a contracting ring for eccentricity mapping (ring width: 0.82 deg; ring was off-screen entirely for 7 s of the 36 s stimulus cycle before reappearing in the periphery) were projected (DLA-G150CL, JVC Ltd.) on a screen using Presentation (NeuroBehavioral Systems). For eccentricity and polar angle mapping, we collected for each subject and each hemifield two data sets, which were averaged for subsequent analyses. During stimulation subjects were instructed to maintain fixation and to report color changes of the central target (diameter: 0.25 deg) via button press. Fixation was monitored during the scans with an MR-compatible eye tracker (Kanowski et al., 2007).

Data Acquisition

To enhance the signal-to-noise-ratio as well as the blood oxygenation level-dependent (BOLD) response, T2*-weighted MR images were acquired during visual stimulation using a Siemens Magnetom 7T MRI system with a 24-channel coil (Hoffmann et al., 2009). Foam padding minimized head motion. A multislice 2D gradient echo EPI sequence (TR 2.4 s; TE 22 ms) was used to measure the BOLD signal as a function of time. Every 2.4 s, 42 approximately axial slices (thickness: 2.5 mm; interleaved slice order without gap) were acquired in an 80 × 80 grid covering a field of view (FOV) of 200 × 200 mm (voxel size: 2.5 × 2.5 × 2.5 mm^3). Functional scans measured at 110 time frames (4.4 min, i.e., 7 1/3 stimulus cycles of 36 s each). The acquired images were motion and distortion corrected online (Zaitsev et al., 2004). Additionally, T1 weighted inhomogeneity corrected MPRAGE MR images (Van de Moortele et al., 2009) were acquired (TR 2.0 s; TE 5.24 s, 176 × 256 × 256 matrix, voxel size: 1 × 1 × 1 mm^3) to create a flattened representation of the cortical gray matter (Teo et al., 1997; Wandell et al., 2000).

Data Analysis

After registration of the T1 weighted images to the T2* weighted images' coordinate frame the fMRI time series were projected onto the flattened representation (Engel et al., 1997). Each voxel's time-series (TS) underwent the following analysis: (1) five temporal samples were discarded from the TS to avoid transient onset artifacts, (2) the TS were divided by the voxel's mean intensity, (3) the TS were filtered with a high-pass cut-off of 4 cycles/scan, (4) the TS of repeated experiments were averaged, (5) Fourier analysis was applied to the TS to obtain the amplitude and phase for each frequency, and (6) the coherence with a sinusoid with a frequency equal to that of the visual stimulation (1/36 Hz), was calculated (Engel et al., 1997). The coherence and phase values in the flattened representation were blurred by convolving a Gaussian kernel (1.7 mm full width at half height) with the complex vector representation of the BOLD response. The blurred phase values that exceeded a coherence threshold that corresponded to $p < 0.001$ (Silver et al., 2005) were then plotted on the flattened representation of the occipital lobe in false color.

Statistics

To assess the correlation of the hemifield maps, the significance of the differences of the z-transformed correlation coefficients (Berens, 2009) from 0 were determined with Student's t test.

PRF Model-Based Analysis

Visual Stimuli

We measured responses to drifting bar apertures at various orientations (Dumoulin and Wandell, 2008); these bar apertures exposed a checkerboard pattern (100% contrast). The bar width subtended one-fourth of the stimulus radius. Four bar orientations and two different motion directions for each bar were used, giving a total of eight different bar configurations within a given scan. Note that the bars were not "phase-encoded" stimuli; there was no repetition of the stimulus because the bars change orientation and motion direction within a scan. The visual stimuli were generated in the Matlab programming environment using the PsychToobox (Brainard, 1997; Pelli, 1997) on a Macintosh G4 Powerbook. Stimuli were displayed with an LCD projector (Stanford: NEC LT158, Magdeburg: DLA-G150CL, JVC Ltd.) with optics that imaged the stimuli onto a projection screen in the bore of the magnet. The stimulus radius was 7.5 deg (Magdeburg setup for AC1) and 14 deg (Stanford setup for AC2) of visual angle. The subjects viewed the display through an angled mirror. Fixation was monitored during the scans with an MR-compatible eye tracker (Magdeburg: Kanowski et al., 2007; Stanford: MagConcept, Redwood City, USA).

Data Acquisition

At Stanford University, magnetic resonance images were acquired with a 3T General Electric Signa scanner and a custom-designed surface coil (Nova Medical, Wilmington, MA) centered over the subject's occipital pole. Foam padding and tape minimized head motion. Functional MR images (TR 1.5 s; TE 30 ms, flip angle 55 deg) were acquired using a self-navigated spiral-trajectory pulse sequence (Glover, 1999; Glover and Lai, 1998) with 20 slices oriented orthogonal to the Calcarine sulcus with no slice gap. The effective voxel size was 2.5 × 2.5 × 3 mm^3 (FOV = 240 × 240 mm). Functional scans measured at 138 time frames (3.5 min). Eight functional scans were performed in each session. T1-weighted anatomical MR images were acquired using a fast spoiled gradient echo (SPGR) sequence prior to the functional scans and using the same slice prescription as the functional scans. In a separate session, high-resolution T1-weighted MRI images were acquired on a 1.5T Signa LX scanner with a vendor-supplied head-coil using a 3D-SPGR pulse sequence (1 echo, minimum TE, flip angle 15 deg, effective voxel size of 0.94 × 0.94 × 1.2 mm^3). At the Magdeburg site, images for fMRI-based pRF-mapping were acquired using a Siemens Magnetom 7T MRI system with the hemifield mapping parameters detailed above, except for the following deviations for similarity to the Stanford parameters: 26 slices, 138 time frames, TR 1.5 s.

Data Analysis

For the data acquired at Stanford University the T1-weighted anatomical MRI data sets were averaged and resampled to a 1 mm^3 isotropic resolution. The surface-coil anatomical MRI, taken at the same time as the functional images, was aligned with the head-coil anatomical MRI using a mutual information method (Ashburner and Friston, 2003; Maes et al., 1997). The functional images and surface-coil anatomical data were acquired in the same session and thus were co-registered. Using the spiral acquisition and small field of view surface-coil limits the size of the distortions between the functional and surface-coil anatomical images. Hence, we used the transformation derived from the surface-coil anatomical to align the functional data to the head-coil anatomical. The preprocessing for the data acquired at Magdeburg University followed that applied to the hemifield mapping data described above. For both data sets, gray and white matter was segmented from the anatomical MRI using custom software and hand-edited to minimize segmentation errors (Teo et al., 1997). The cortical surface was reconstructed at the white/gray matter border and rendered as a smoothed 3D surface (Wandell et al., 2000). The first eight time frames of each functional run were discarded due to start-up magnetization transients. Head movement and motion artifacts within and between scans were measured (Nestares and Heeger, 2000). With all subjects, the scans contained minimal head motion (less than one voxel), so no motion correction algorithm was applied. The population receptive field (pRF) is defined as the region of visual space that stimulates the recording site (Dumoulin and Wandell, 2008; Jancke et al., 2004; Victor et al., 1994). We used a model-based method to estimate the properties of the pRF. Details of the pRF analysis and rationale are provided in our previous study (Dumoulin and Wandell, 2008). Briefly, for each cortical location, we predicted the fMRI response using a model of the pRF. The conventional model consists of a 2D Gaussian. The predicted fMRI time series is calculated by a convolution of the model pRF with the stimulus sequence and the BOLD hemodynamic response function (HRF); the pRF parameters for each cortical location minimize the sum of squared errors between the predicted and observed fMRI time-series for all stimuli. Here, we tested several other models of the pRF in addition to the conventional 2D Gaussian. These models consisted of two 2D Gaussians mirrored around the x axis, y axis or fixation. Because the two Gaussians are linked to each other, these models have the same degrees of freedom as the conventional one Gaussian pRF model. But unlike the conventional model, these alternate models represent two distinct regions of visual space within each cortical location.

DTI and Tractography

Data Acquisition

DTI data were acquired on a 1.5T Signa LX (Signa CVi; GE Medical Systems, Milwaukee, WI) with a self-shielded, high-performance gradient system capable of providing a maximum gradient strength of 50 mT/m at a gradient rise time of 268 µs for each of the gradient axes. A standard quadrature head coil was used for excitation and signal reception. The DTI protocol used eight 90 s whole-brain scans. The pulse sequence was a diffusion-weighted, single-shot, spin-echo, echo-planar imaging sequence (echo time, 63 ms; repetition time, 6 s; field of view, 260 mm; matrix size, 128 × 128; bandwidth, ± 110 kHz; partial k-space acquisition). We acquired 48–54 axial, 2-mm-thick slices (no skip) for two b-values, $b = 0$ and $b = 800$ s/mm^2. The high b-value was obtained by applying gradients along 12 different diffusion directions (six noncollinear directions). Two gradient axes were energized simultaneously to minimize echo time. The polarity of the effective diffusion-weighting gradients was reversed for odd repetitions to reduce cross-terms between diffusion gradients and imaging and background gradients.

Data Analysis

Eddy current distortions and subject motion were removed by a 14-parameter constrained nonlinear coregistration based on the expected pattern of eddy-current distortions given the phase-encode direction of the acquired data (Rohde et al., 2004). Each diffusion-weighted image was then registered to the mean of the (motion-corrected) non-diffusion-weighted images using a two-stage coarse-to-fine approach that maximized the normalized mutual information. The mean of the non-diffusion-weighted images was also automatically aligned to the T1 image using a rigid body mutual information algorithm. All raw images from the diffusion sequence were then re-sampled to 2 mm isotropic voxels by combining the motion correction, eddy-current correction, and anatomical alignment transforms into one omnibus transform. and resampling the data using a seventh-order b-spline algorithm based on code from SPM5 (Friston and Ashburner, 2004) was done. An eddy-current intensity correction (Rohde et al., 2004, 2005) was also applied to the diffusion weighted images at this resampling stage. The rotation component of the omnibus coordinate transform was applied to the diffusion-weighting gradient directions to preserve their orientation with respect to the resampled diffusion images. The tensors were fit using a least-squares algorithm. The eigenvalue decomposition of the diffusion tensor was computed, and the fractional anisotropy was calculated from the eigenvalues (Basser, 1995; Basser and Pierpaoli, 1996). The FA is the normalized standard deviation of the three eigenvalues and indicates the degree to which the isodiffusion ellipsoid is anisotropic. The mean diffusivity (MD) is the mean of the three eigenvalues, which is equivalent to one-third of the trace of the diffusion tensor.

Tractography

We identified the fibers using the probabilistic ConTrack algorithm (Sherbondy et al., 2008a). This method is designed to find the most likely pathway between two regions of interest and has been validated against gold-standard post-mortem tract-tracing methods (Sherbondy et al., 2008b).

Optic Tract. Large ROIs that contain the optic chiasm, including both optic tract origins, were positioned on T1 maps of each subject, centered at the infundibular stem of the hypothalamus. This way we were able to compare the optic tracts of the subject who lack an optic chiasm and the controls. Both LGNs were also defined anatomically on the T1 maps, and their volumes were standardized to 485 mm^3. ConTrack calculated the most likely pathway between the ROIs of the optic chiasm and the LGN. A set of 5,000 potential pathways were generated and the top 10% (500) highest scores fibers were chosen as the most likely pathways connecting these two regions.

Optic Radiation. In this case, we estimated the optic radiation as the most likely pathway between the LGN ROI and each hemisphere's Calcarine. The Calcarine ROIs were delineated for each subject on their T1 maps. We sampled 100,000 possible pathways and estimated the optic radiation as the top 1% (1000) of these pathways. A few clearly misidentified fibers were eliminated (Sherbondy et al., 2008b).

Occipital Callosal Fibers. To analyze diffusion properties in the corpus callosum, we adopted parts of the corpus callosum segmentation procedure described by Dougherty et al. (2007) and Huang et al. (2005). We manually defined an occipital ROI within the white matter and a corpus callosum ROI for each subject. We sampled 100,000 fibers that pass through both ROIs and estimated the 1% (1,000) of these generated pathways. We then measured the cross-sectional area of these callosal-occipital fibers in the plane of the corpus callosum. The process was performed on each hemisphere separately; we also estimated the cross-sectional area of the whole corpus callosum.

SUPPLEMENTAL INFORMATION

Supplemental Information includes two figures and can be found with this article online at http://dx.doi.org/10.1016/j.neuron.2012.05.026.

ACKNOWLEDGMENTS

We thank the subjects for their patience and cooperation. We would also like to express our appreciation to Greg Corrado and Julian Brown for the use of their eye-tracker and their help. This work was supported by German Research Foundation (DFG) HO 2002/10-1 (M.B.H.), NIH EY 03164 (B.A.W.), and Marie Curie Reintegration Grant #231027 (S.O.D.).

Accepted: May 20, 2012
Published: August 8, 2012

REFERENCES

Amano, K., Wandell, B.A., and Dumoulin, S.O. (2009). Visual field maps, population receptive field sizes, and visual field coverage in the human MT+ complex. J. Neurophysiol. *102*, 2704–2718.

Apkarian, P., Reits, D., Spekreijse, H., and Van Dorp, D. (1983). A decisive electrophysiological test for human albinism. Electroencephalogr. Clin. Neurophysiol. *55*, 513–531.

Apkarian, P., Bour, L., and Barth, P.G. (1994). A unique achiasmatic anomaly detected in non-albinos with misrouted retinal-fugal projections. Eur. J. Neurosci. *6*, 501–507.

Apkarian, P., Bour, L.J., Barth, P.G., Wenniger-Prick, L., and Verbeeten, B., Jr. (1995). Non-decussating retinal-fugal fibre syndrome. An inborn achiasmatic malformation associated with visuotopic misrouting, visual evoked potential ipsilateral asymmetry and nystagmus. Brain *118*, 1195–1216.

Ashburner, J., and Friston, K.J. (2003). Rigid body registration. In Human Brain Function, W.D. Penny, ed. (San Diego, CA: Academic Press).

Baseler, H.A., Brewer, A.A., Sharpe, L.T., Morland, A.B., Jägle, H., and Wandell, B.A. (2002). Reorganization of human cortical maps caused by inherited photoreceptor abnormalities. Nat. Neurosci. *5*, 364–370.

Basser, P.J. (1995). Inferring microstructural features and the physiological state of tissues from diffusion-weighted images. NMR Biomed. *8*, 333–344.

Basser, P.J., and Pierpaoli, C. (1996). Microstructural and physiological features of tissues elucidated by quantitative-diffusion-tensor MRI. J. Magn. Reson. *111*, 209–219.

Berens, B. (2009). CircStat: a MATLAB toolbox for circular statistics. J. Stat. Softw. *31*, 1–21.

Brainard, D.H. (1997). The psychophysics toolbox. Spat. Vis. *10*, 433–436.

DeYoe, E.A., Carman, G.J., Bandettini, P., Glickman, S., Wieser, J., Cox, R., Miller, D., and Neitz, J. (1996). Mapping striate and extrastriate visual areas in human cerebral cortex. Proc. Natl. Acad. Sci. USA *93*, 2382–2386.

Dougherty, R.F., Ben-Shachar, M., Deutsch, G.K., Hernandez, A., Fox, G.R., and Wandell, B.A. (2007). Temporal-callosal pathway diffusivity predicts phonological skills in children. Proc. Natl. Acad. Sci. USA *104*, 8556–8561.

Dumoulin, S.O., and Wandell, B.A. (2008). Population receptive field estimates in human visual cortex. Neuroimage *39*, 647–660.

Engel, S.A., Rumelhart, D.E., Wandell, B.A., Lee, A.T., Glover, G.H., Chichilnisky, E.J., and Shadlen, M.N. (1994). fMRI of human visual cortex. Nature *369*, 525.

Engel, S.A., Glover, G.H., and Wandell, B.A. (1997). Retinotopic organization in human visual cortex and the spatial precision of functional MRI. Cereb. Cortex *7*, 181–192.

Friston, K.J., and Ashburner, J. (2004). Generative and recognition models for neuroanatomy. Neuroimage *23*, 21–24.

Glover, G.H. (1999). Simple analytic spiral K-space algorithm. Magn. Reson. Med. *42*, 412–415.

Glover, G.H., and Lai, S. (1998). Self-navigated spiral fMRI: interleaved versus single-shot. Magn. Reson. Med. *39*, 361–368.

Guillery, R.W. (1986). Neural abnormalities of albinos. Trends Neurosci. *9*, 364–367.

Guillery, R.W., Hickey, T.L., Kaas, J.H., Felleman, D.J., Debruyn, E.J., and Sparks, D.L. (1984). Abnormal central visual pathways in the brain of an albino green monkey (*Cercopithecus aethiops*). J. Comp. Neurol. *226*, 165–183.

Harvey, B.M., and Dumoulin, S.O. (2011). The relationship between cortical magnification factor and population receptive field size in human visual cortex: constancies in cortical architecture. J. Neurosci. *31*, 13604–13612.

Hoffmann, M.B., Tolhurst, D.J., Moore, A.T., and Morland, A.B. (2003). Organization of the visual cortex in human albinism. J. Neurosci. *23*, 8921–8930.

Hoffmann, M.B., Seufert, P.S., and Schmidtborn, L.C. (2007). Perceptual relevance of abnormal visual field representations: static visual field perimetry in human albinism. Br. J. Ophthalmol. *91*, 509–513.

Hoffmann, M.B., Stadler, J., Kanowski, M., and Speck, O. (2009). Retinotopic mapping of the human visual cortex at a magnetic field strength of 7T. Clin. Neurophysiol. *120*, 108–116.

Huang, H., Zhang, J., Jiang, H., Wakana, S., Poetscher, L., Miller, M.I., van Zijl, P.C., Hillis, A.E., Wytik, R., and Mori, S. (2005). DTI tractography based parcellation of white matter: application to the mid-sagittal morphology of corpus callosum. Neuroimage *26*, 195–205.

Huberman, A.D., Feller, M.B., and Chapman, B. (2008). Mechanisms underlying development of visual maps and receptive fields. Annu. Rev. Neurosci. *31*, 479–509.

Jancke, D., Chavane, F., Naaman, S., and Grinvald, A. (2004). Imaging cortical correlates of illusion in early visual cortex. Nature *428*, 423–426.

Kanowski, M., Rieger, J.W., Noesselt, T., Tempelmann, C., and Hinrichs, H. (2007). Endoscopic eye tracking system for fMRI. J. Neurosci. Methods *160*, 10–15.

Klemen, J., Hoffmann, M.B., and Chambers, C.D. (2012). Cortical plasticity in the face of congenitally altered input into V1. Cortex. Published online March 23, 2012. http://dx.doi.org/10.1016/j.cortex.2012.03.012.

Levin, N., Dumoulin, S.O., Winawer, J., Dougherty, R.F., and Wandell, B.A. (2010). Cortical maps and white matter tracts following long period of visual deprivation and retinal image restoration. Neuron *65*, 21–31.

Maes, F., Collignon, A., Vandermeulen, D., Marchal, G., and Suetens, P. (1997). Multimodality image registration by maximization of mutual information. IEEE Trans. Med. Imaging *16*, 187–198.

Muckli, L., Naumer, M.J., and Singer, W. (2009). Bilateral visual field maps in a patient with only one hemisphere. Proc. Natl. Acad. Sci. USA *106*, 13034–13039.

Nestares, O., and Heeger, D.J. (2000). Robust multiresolution alignment of MRI brain volumes. Magn. Reson. Med. *43*, 705–715.

Pelli, D.G. (1997). The VideoToolbox software for visual psychophysics: transforming numbers into movies. Spat. Vis. *10*, 437–442.

Petros, T.J., Rebsam, A., and Mason, C.A. (2008). Retinal axon growth at the optic chiasm: to cross or not to cross. Annu. Rev. Neurosci. *31*, 295–315.

Prakash, S., Dumoulin, S.O., Fischbein, N., Wandell, B.A., and Liao, Y.J. (2010). Congenital achiasma and see-saw nystagmus in VACTERL syndrome. J. Neuroophthalmol. *30*, 45–48.

Rohde, G.K., Barnett, A.S., Basser, P.J., Marenco, S., and Pierpaoli, C. (2004). Comprehensive approach for correction of motion and distortion in diffusion-weighted MRI. Magn. Reson. Med. *51*, 103–114.

Rohde, G.K., Barnett, A.S., Basser, P.J., and Pierpaoli, C. (2005). Estimating intensity variance due to noise in registered images: applications to diffusion tensor MRI. Neuroimage *26*, 673–684.

Sereno, M.I., Dale, A.M., Reppas, J.B., Kwong, K.K., Belliveau, J.W., Brady, T.J., Rosen, B.R., and Tootell, R.B. (1995). Borders of multiple visual areas in humans revealed by functional magnetic resonance imaging. Science *268*, 889–893.

Sherbondy, A.J., Dougherty, R.F., Ben-Shachar, M., Napel, S., and Wandell, B.A. (2008a). ConTrack: finding the most likely pathways between brain regions using diffusion tractography. J. Vis. *8*, 11–16.

Sherbondy, A.J., Dougherty, R.F., Napel, S., and Wandell, B.A. (2008b). Identifying the human optic radiation using diffusion imaging and fiber tractography. J. Vis. *8*, 11.

Silver, M.A., Ress, D., and Heeger, D.J. (2005). Topographic maps of visual spatial attention in human parietal cortex. J. Neurophysiol. *94*, 1358–1371.

Teo, P.C., Sapiro, G., and Wandell, B.A. (1997). Creating connected representations of cortical gray matter for functional MRI visualization. IEEE Trans. Med. Imaging *16*, 852–863.

Van de Moortele, P.F., Auerbach, E.J., Olman, C., Yacoub, E., Uğurbil, K., and Moeller, S. (2009). T1 weighted brain images at 7 Tesla unbiased for Proton Density, T2* contrast and RF coil receive B1 sensitivity with simultaneous vessel visualization. Neuroimage *46*, 432–446.

Victor, J.D., Purpura, K., Katz, E., and Mao, B. (1994). Population encoding of spatial frequency, orientation, and color in macaque V1. J. Neurophysiol. *72*, 2151–2166.

Victor, J.D., Apkarian, P., Hirsch, J., Conte, M.M., Packard, M., Relkin, N.R., Kim, K.H., and Shapley, R.M. (2000). Visual function and brain organization in non-decussating retinal-fugal fibre syndrome. Cereb. Cortex *10*, 2–22.

Wandell, B.A., Chial, S., and Backus, B.T. (2000). Visualization and measurement of the cortical surface. J. Cogn. Neurosci. *12*, 739–752.

Wandell, B.A., Dumoulin, S.O., and Brewer, A.A. (2007). Visual field maps in human cortex. Neuron *56*, 366–383.

Williams, R.W., Hogan, D., and Garraghty, P.E. (1994). Target recognition and visual maps in the thalamus of achiasmatic dogs. Nature *367*, 637–639.

Winawer, J., Horiguchi, H., Sayres, R.A., Amano, K., and Wandell, B.A. (2010). Mapping hV4 and ventral occipital cortex: the venous eclipse. J. Vis. *10*, 1–22.

Wolynski, B., Kanowski, M., Meltendorf, S., Behrens-Baumann, W., and Hoffmann, M.B. (2010). Self-organisation in the human visual system—visuo-motor processing with congenitally abnormal V1 input. Neuropsychologia *48*, 3834–3845.

Zaitsev, M., Hennig, J., and Speck, O. (2004). Point spread function mapping with parallel imaging techniques and high acceleration factors: fast, robust, and flexible method for echo-planar imaging distortion correction. Magn. Reson. Med. *52*, 1156–1166.